Neutral pressure dynamics in the upper plenums in the DIII-D tokamak

R. Maingi[1], J.G. Watkins[2], M.A. Mahdavi and R.J. Colchin[1]

General Atomics, San Diego, California, USA

[1] Oak Ridge National Laboratory, Oak Ridge, Tennessee, USA
[2] Sandia National Laboratories, Albuquerque, New Mexico, USA

E-mail: rmaingi@pppl.gov

Abstract
We present the dependence of the neutral pressure rise on strike point geometry in the inner and outer plenums of the upper divertor in the DIII-D tokamak. The upper outer plenum pressure increases in the proximity of the plenum opening in a manner similar to previous reports of the lower outer plenum pressure. The inner plenum pressure measurement is modulated up to a factor of two by edge-localized modes (ELMs) particle flux, due to the small plenum volume and resulting short equilibration time constant. Reasonable agreement is obtained between the measured dependence of the outer plenum pressure on strike point position and simulations with an analytic neutral transport model, using the time-averaged (i.e. long compared with the ELM period) divertor profiles as inputs. The modelling of inner plenum pressure data with time-averaged profiles traces through the middle of the data range. In addition, modelling with two other sets of profiles, one averaged in the vicinity of ELMs and the other between ELMs, covers the upper and lower envelopes of the data. These new data sets represent an independent test and the agreement confirms that the basic physics in the model is responsible for the dependence of pressure rise on strike point geometry in the long mean free path limit.

PACS numbers: 52.40.Hf, 52.55.Fa

1. Introduction

Current drive research is a critical component of the advanced tokamak programme in DIII-D. Because driven current increases with decreasing density, density control is a crucial element of DIII-D research. The divertor pumping rate has been successively increased with stepwise modifications over the last ten years in DIII-D. The original lower divertor plenum and cryopump were installed in stages by 1993, leading to density control in H-mode plasmas [1]. The upper outer plenum and pump were installed in 1998, allowing the pumping of higher triangularity plasmas [2]. Finally, the upper inner plenum and pump were installed [3] in 2000, allowing the pumping of the upper inner strike point (ISP) as well, and leading to the present upper divertor hardware configuration (figure 1). Particle balance has historically been used in DIII-D (e.g. [4–6] and references therein) as a way of measuring the effect of the pumps on the plasma and the wall conditions. In those studies, the particle exhaust rate was estimated as the product of the pumping speed and plenum neutral pressure. However, it was determined rather early that both the pressure [7] and, hence, the exhaust rate [8] depend on the proximity of the strike point to the plenum opening. Hence, to optimize the

exhaust rate and density control, it is necessary to understand the plenum pressure rise characteristics and its dependence on local divertor plasma profiles and geometry. The remainder of this paper compares and contrasts the characteristics of the pressure rise in the upper plenums and also compares the measured pressure with an analytic model [9] of neutral recycling and transport into the plenums. This model has previously been used to simulate data from the lower divertor outer plenum. The new data provide a fresh test of the model physics in several ways. We note that other authors have previously used analytic or semi-analytic models to examine pressure rise in plenums with reasonable success [10, 11].

2. Inner and outer plenum pressure measurements

The inner and outer plenums in the upper divertor are shown schematically in figure 1. The most obvious difference between these plenums are their relative sizes: the inner one has a volume V of $\sim 0.15\,\mathrm{m}^3$ and the outer one, $\geqslant 1\,\mathrm{m}^3$. Note that the inner plenum is small, by design, to minimize the impact on the vacuum vessel volume available for the plasma. The pumping speed of the inner pump (S_p) and
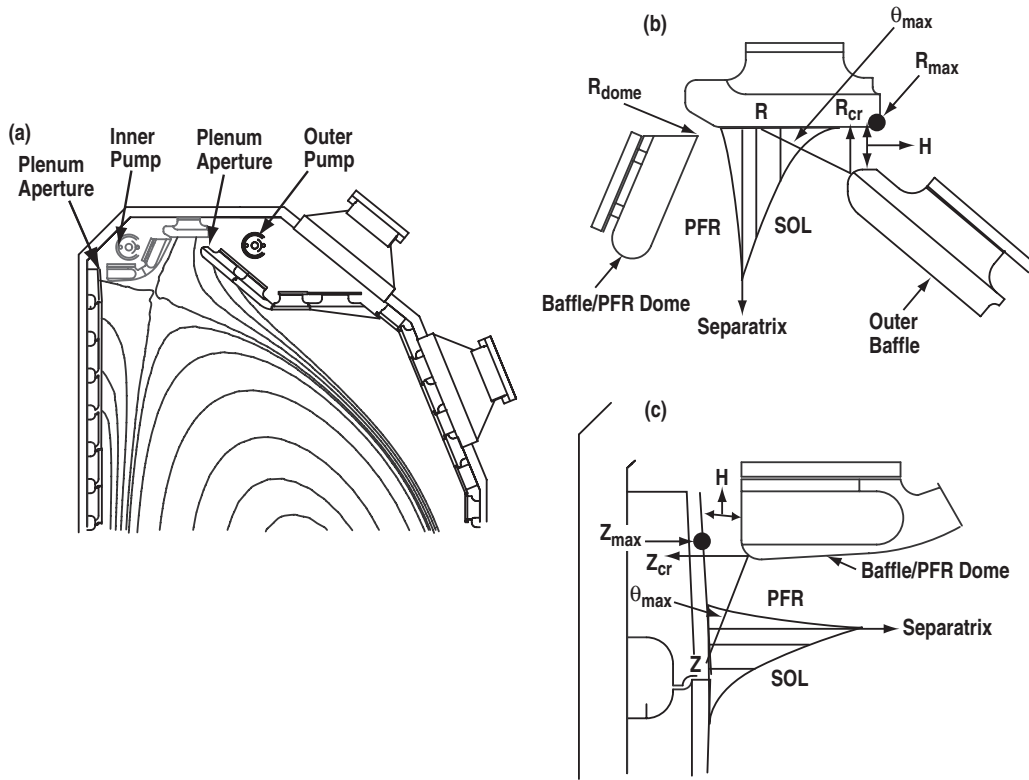
Figure 1. (*a*) Schematic of the inner and outer upper pumps and plenums. The plenum apertures and pump locations are indicated; (*b*) schematic representation of pump plenum entrance and model inputs for upper outer plenum; (*c*) schematic representation of pump plenum entrance and model inputs for upper inner plenum. The PFR is the space between the inner and outer strike points. All symbols are defined in [9]. Note that $R_{cr} = R_{pl}$ and $Z_{cr} = Z_{pl}$.

the conductance (C) were measured in off-line tests to be $\sim$18 m^3 s^{-1} each, whereas the pumping speed of the outer pump and its conductance were measured at $\sim$40 m^3 s^{-1} each. The time constant of each plenum with pumps turned on (τ_{pl}) is given by $\tau_{pl} = V/(S_p + C)$, which yields $\sim$4 ms for the inner plenum and $\geqslant$12 ms for the outer plenum. Thus, we expect that the inner plenum pressure measurement will respond more rapidly to transient events than the outer plenum, provided the pressure gauge time response is sufficiently fast. A second difference in the pumping geometry is that the outer plenum samples the Scrape-Off Layer (SOL), separatrix, and then the private flux region (PFR) as the outer strike point (OSP) is moved toward the plenum opening from small major radius to large major radius (figure 1(*b*)). In contrast, the inner plenum samples first the PFR, the separatrix, and then the SOL as the strike point height is increased along the inner wall. These distinctions translate into different dependences of pressure rise as a function of the strike point position relative to the plenum opening. We discuss the outer plenum first because it is similar in geometry to several published reports of the lower, outer plenum, with the exception that the upper, outer divertor is generally described as more 'closed' [12] than the lower, outer divertor.

The discharge parameters during a typical OSP sweep are shown in figure 2. The discharge had the following characteristics: plasma current (I_p) = 1.2 MA, neutral beam injected (NBI) power = 4.9 MW, toroidal field (B_t) = 2.1 T and the ion grad-B drift was toward the X-point in the upper single-null configuration. Also we note that the cryopump was
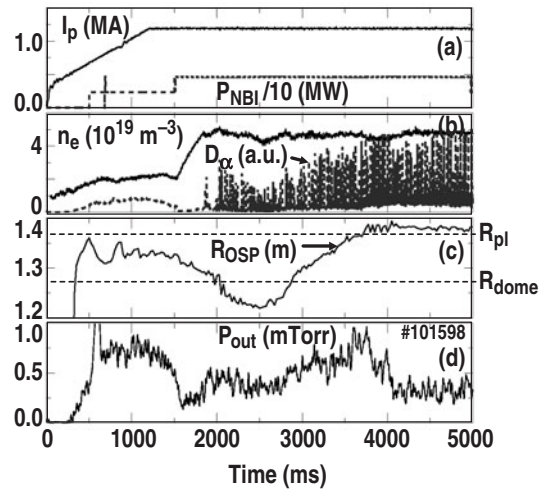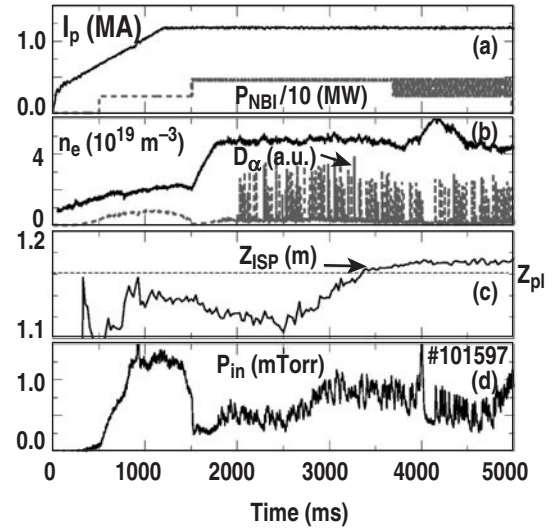

Figure 2. Characteristics of ELMy discharge with OSP (radial) sweep and cryopump active. The radius of the plenum opening (R_{pl}) and private region dome (R_{dome}) are indicated. Oscillations in the pressure are not directly correlated with ELMs.

active. Panel 2(*b*) shows that the line density was maintained at 5×10^{19} m^{-3} with gas puffing, and that type I edge-localized modes (ELMs) were observed in the upper divertor D$_\alpha$ emission. Panel 2(*c*) shows the extent of the OSP sweep, from $R = 1.22$ m (2200 ms) to $R = 1.39$ m (4000 ms). For reference, the plenum opening is at $R_{pl} = 1.37$ m and the PFR dome extends out to $R_{dome} = 1.28$ m.

Note that the line density would normally decrease during the sweep, as the strike point approached the plenum opening. This density reduction has been attributed to an increase in the plenum capture efficiency (fraction of target recycling flux transported into the plenum) as the strike point approached the plenum opening [7], resulting in a reduced recycling flux and core fuelling rate. However, our goal here is to understand the effects of geometry on the pressure rise. Therefore, temporal changes to the density were minimized by using gas-puffing feedback to control line-averaged density during the strike point sweep. It is well documented [13] that the divertor profiles have a strong dependence on edge density; thus, allowing the density to drop during the sweep would make it difficult to separate the density dependence and the geometry dependence of the plenum pressure rise. Panel 2(d) shows the time dependence of the plenum pressure, measured by a fast time-response ionization gauge [14–16]. Note that the plenum pressure rises during the OSP sweep, reaching a maximum approximately when the OSP radius approaches the plenum opening, R_{pl}, at ~3800 ms. Note also that the plenum pressure falls when the OSP goes up on the side of the plenum opening beyond ~3800 ms. We mention here that some of the larger, fast modulations in plenum pressure during the strike point sweep are not correlated in time with the ELMs but are apparently electronic noise (approximately ±15%), the level of which can be observed at e.g. $t = 1000$ ms. It is unclear whether this noise is related to plasma turbulence or the sensitivity of the electronics to electromagnetic fields. Generally speaking, however, the basic characteristics are similar to those previously reported [17] of the outer, lower original plenum in DIII-D.

In comparison, the inner plenum neutral pressure characteristics during a typical ISP sweep are shown in figure 3. This discharge had the inner cryopump active and also used gas-puffing feedback to control line-averaged density. It had the same programmed characteristics as the previous discharge, namely: $I_p = 1.2$ MA, $P_{NBI} = 4.9$ MW, $B_t = 2.1$ T, and the ion grad-B drift was toward the X-point in the upper single null. Panel 3(b) shows that the line-averaged density was maintained at 5×10^{19} m^{-3}, and that upper divertor D_α emission had type I ELMs (frequency ~60 Hz) until the NBI source dropout at $t = 3700$ ms. After 3700 ms, the ELM frequency initially decreased allowing the line density to rise up to 6×10^{19} m^{-3} before feedback control was restored. Thus in the analysis section, we will consider only the time of constant NBI input power, i.e. from 2400 to 3700 ms. Panel 3(c) shows the extent of the ISP sweep vertically along the inner wall, from $Z = 1.1$ m (2500 ms) to $Z = 1.18$ m (4000 ms). For reference, the plenum opening is at $Z_{pl} = 1.161$ m. Panel 3(d) shows the time dependence of the plenum pressure measured by a fast time-response ionization gauge similar to the outer plenum gauge. One of the most significant features of the plenum pressure data is the factor of two signal increase during the lifetime of ELMs relative to the data between ELM events. This modulation is clearly in phase with the ELMs as shown in figure 4. Note that D_α and the ion saturation current from a Langmuir probe near the plenum opening are in phase, as expected. The pressure rises within a few milliseconds of arrival of the ELM particle flux into the plenum throat, consistent with the ~4 ms plenum

Figure 3. Characteristics of discharge with ISP (vertical) sweep and cryopump active. The vertical location of the plenum opening (Z_{pl}) is indicated. Oscillations in the pressure are synchronized with the ELMs.
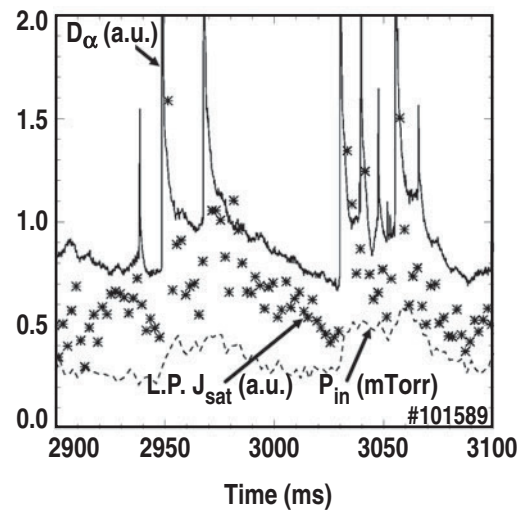
Figure 4. Time dependence of ion saturation current, D_α, and pressure rise in inner plenum, showing synchronization of pressure rise with ELMs. This discharge is similar to the one from figure 3 except that density feedback was turned off.

response time above. The pressure decays on a longer, 15–20 ms, timescale, but this is apparently due to the decay time constant of the Langmuir probe flux in figure 4, which is probably related to dynamic hydrogen desorption caused by ELMs and disruptions [18]. Thus, simulations of the inner plenum pressure rise must consider both a high particle flux due to ELMs (averaged suitably over 1 to 2 plenum time constants), and the lower particle flux between ELMs. In contrast to the outer plenum gauge, we note that these modulations in the inner plenum pressure data are not due to electronic noise, which is typically <5% [e.g. panel 3(d) at 1000 ms]. Note that the upper envelope (e.g. maximum values) of the plenum pressure began to rise during the ISP sweep, approximately reaching a maximum when ISP height approached within a few centimetres of the plenum opening, Z_{pl}, at ~3100 ms. As the

strike point height continued to increase, however, the upper (and lower) range of the plenum pressure decayed on a very slow timescale as compared with the outer plenum data.

3. Pressure simulations

We will analyse the dependence of pressure on divertor parameters and geometry with a slightly modified version of an analytic model used [9] previously for DIII-D data. Model modifications will be discussed for each plenum simulation. In brief, the original model considers first flight neutral transport of the recycled ion flux off the rough graphite tile surfaces. The plenum is considered as an aperture with critical radius $R_{cr} = R_{pl}$ (or $Z_{cr} = Z_{pl}$ for the inner pump), and the maximum radius of the ion flux before striking the side of the plenum opening is given by R_{max} (Z_{max} for the inner pump), which can be greater (less) than R_{cr} (Z_{cr} for the inner pump) due to flux surface curvature toward (away) from the plenum opening. The probability of a neutral entering the plenum is given as the product of the solid angle of the plenum opening and probability that the neutral would not be ionized along the path length to the opening. Both Franck–Condon and reflected atoms are considered in computing the neutral kinetic energy and velocity. Finally, the neutral pressure is computed as the ratio of neutral flux into the plenum and the sum of the cryopump pumping speed and plenum conductance. The divertor ion flux and electron density and temperature profiles are required inputs, as is the time-dependent magnetic equilibrium generated by the EFITD code [19].

3.1. Outer divertor

The present upper, outer divertor has an array of seven domed Langmuir probes embedded in the large, single graphite tile to provide high spatial resolution measurements of the target n_e, T_e and $\Gamma_{||}$ profiles [20]. The design of these dome-shaped probes is similar to the lower divertor probes [21]. The bias on these probes is swept to obtain an I/V curve every 1 ms.

We discuss here the impact of the ELMs on these measurements and the meaning of 'profiles averaged over ELMs'. The probes' I/V characteristics are usually altered as the ELM occurs and cannot be analysed for profiles; however, the remainder of the characteristics (including just after the divertor particle flux spike) can be analysed to obtain profiles. This limitation does not significantly impact our analysis of the outer divertor data because the duration of the ELM flux is short compared with the outer plenum equilibration time constant $\sim$12 ms. We expand the inner divertor analysis in the next section to consider this effect because of the shorter inner plenum time constant $\sim$4 ms.

Plasma profiles are measured during the OSP sweep. These time-dependent profiles are converted to spatial profiles relative to the separatrix location by using the EFIT equilibrium reconstruction at each profile time. The spatial profiles are then

fitted to the functional forms:

$$f(x) = \begin{cases} (A_0 - B_0)\exp\left(\dfrac{-x}{\lambda_{SOL,1}}\right) + B_0 \\ \qquad \text{for } 0 < x < (\Delta_{SOL,1} - \Delta_{sep}), \\ A_1\exp\left[\dfrac{-(x - \Delta_{SOL,1})}{\lambda_{SOL,2}}\right] + B_0 \\ \qquad \text{for } x > (\Delta_{SOL,1} - \Delta_{sep}), \\ (A_0 - B_1)\exp\left(\dfrac{x}{\lambda_{PFR}}\right) + B_1 \qquad \text{for } x < 0, \end{cases} \tag{1}$$

where $x = (R - R_{sep} - \Delta_{sep})$.

In this functional form, the parameters are interpreted as:

A_0—The maximum profile value (m^{-2} s^{-1}, m^{-3} and eV for $\Gamma_{||}$, n_e, and T_e, in that order).

$\lambda_{SOL,1}$ and $\lambda_{SOL,2}$—Two separate scale lengths on the SOL side of the separatrix.

$\Delta_{SOL,1}$—The location at which the profile goes from scale length $\lambda_{SOL,1}$ to $\lambda_{SOL,2}$.

A_1—The value at $\Delta_{SOL,1}$ for profile continuity $= (A_0-B_0)\times \exp(-\Delta_{SOL,1}/\lambda_{SOL,1}) + B_0$.

λ_{PFR}—The scale length on the PFR side of the separatrix.

Δ_{sep}—The spatial offset of the peak value from the separatrix location.

B_0—The flat baseline value in the SOL.

B_1—The flat baseline value in the PFR.

We determined that the divertor plasma profiles were changing modestly during the strike point sweep and, thus, used two sets of profiles, in the simulations shown below, to illustrate the sensitivity of the calculations to these changes. The values of the fitted profile parameters are displayed in tables 1 and 2. The main changes were to the T_e profile and the region in the far SOL for the $\Gamma_{||}$ profile. More precisely, a long tail in the $\Gamma_{||}$ profile was observed when the strike point was far away from the plenum opening, and this tail disappeared as the strike point was moved closer to the plenum opening.

Other inputs needed for the model simulation are the plenum opening height ($H = 0.038$ m) and R_{max}. In the original version of the model, R_{max} was fixed at the maximum radial value of the flux surface when the OSP was deep in the plenum opening, just before going on the side of the plenum entrance. This approximation yielded an $R_{max} > R_{cr}$ for all strike point locations. In fact, however, when the OSP is far away from the plenum opening, the flux surfaces become nearly vertical and $R_{max} \sim R_{cr}$. Hence, we have fitted the experimental dependence of R_{max} on the OSP location with a second-order polynomial, and this fit was used in the simulations. The physical effect of this refinement is that the solid angle falls off more quickly than previously for OSP locations far away from the plenum opening. This, in turn, leads to a moderately stronger dependence of the computed pressure on OSP location relative to the plenum opening.

Comparison of the simulations (using the profiles in table 1 (dot/chain dot curve) and table 2 (dash/solid curve) in the variable ion current model of [9]) with the pressure data as a function of OSP location is shown in figure 5. Note that the dotted portion of the dot/chain dot curve applies for $1.28 < R_{OSP} < 1.33$ m. Similarly, the solid portion of the

Table 1. Plasma profile scale lengths for outer plenum simulation (#101598) for strike point radii between 1.28 and 1.33 m (2950 to 3250 ms). The time over which the profile was acquired was long compared with the mean ELM time, and thus is averaged over ELMs.

Quantity	A_0	$\lambda_{SOL,1}$ (m)	$\lambda_{SOL,2}$ (m)	$\Delta_{SOL,1}$ (m)	λ_{PFR} (m)	Δ_{sep} (m)	B_0	B_1
$\Gamma_{\parallel}$ (MA m^{-2})	0.28	0.008	0.005	0.04	0.006	0	0.08, 0.025[a]	0
n_e (10^{19} m^{-3})	2.8	0.015	—	—	0.005	0.006	1.0	0
T_e (eV)	39	0.015	—	—	0.005	0.006	14	5

[a] Indicates that the plasma had two separate baseline values in the SOL, the first was applicable for $x < (\Delta_{SOL,1} - \Delta_{sep})$ whereas the second value applied for the rest of the SOL.

Table 2. Plasma profile scale lengths for outer plenum simulation (#101598) for strike point radii between 1.33 and 1.37 m (3250 to 3700 ms). The time over which the profile was acquired was long compared with the mean ELM time and thus is averaged over ELMs.

Quantity	A_0	$\lambda_{SOL,1}$ (m)	$\lambda_{SOL,2}$ (m)	$\Delta_{SOL,1}$ (m)	λ_{PFR} (m)	Δ_{sep} (m)	B_0	B_1
$\Gamma_{\parallel}$ (MA m^{-2})	0.28	0.015	—	—	0.006	0	0	0
n_e (10^{19} m^{-3})	2.8	0.025	—	—	0.01	0.006	0	0
T_e (eV)	28	0.005	—	—	0.002	0.006	10	10
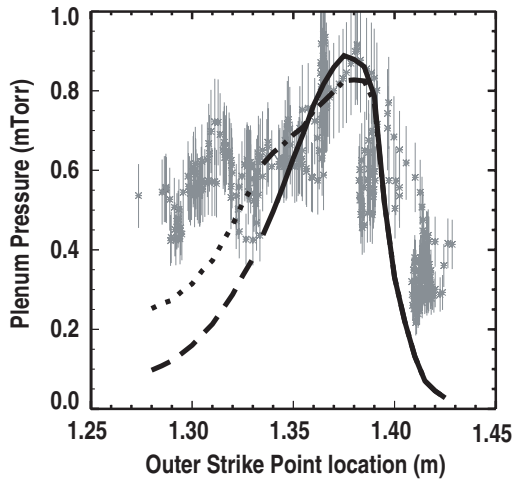
Figure 5. Simulation of the outer plenum pressure during the OSP sweep of the discharge in figure 2. Two curves are shown to account for profile measurements at different times as described in tables 1 and 2. The dotted portion of the dot/chain dot curve and the solid portion of the dash/solid curve represent the calculation based on the profile measurement during that duration of the OSP sweep. Both curves are shown over the entire strike point range to demonstrate model sensitivity to profile variations.

dash/solid curve applies for $1.33 < R_{OSP} < 1.37$ m. We note that the difference between these two simulations is caused by the presence of the baselines in the particle flux profile (see tables 1 and 2). Both simulations are shown over the entire calculation range to demonstrate the sensitivity of the calculations to these profile differences. The agreement between the model calculations and data is generally good, e.g. both the peak pressure value and location, as well as the pressure falloff within ± 2 cm of the peak location are well matched. This good agreement is, perhaps, not unexpected since the basic geometry of the upper outer plenum is similar to the lower outer plenum, which was successfully modelled in [9]. Still, it represents an important validation of the analytic model since an entirely new set of diagnostics, a new pump and plenum, and a different shape (i.e. upper single null) were used. For completeness, we note that the OSP location when

on the side of the plenum opening was extrapolated using $R_{OSP} \sim R_{pl} + 0.5 \times (Z_{floor} - Z_{OSP})$, which equates to a flux surface angle $\sim 26°$ with respect to the horizontal plate. The extrapolation angle is based on the flux surface angle when the strike point is at the maximum radial location before striking the side of the plenum opening.

The agreement between the simulations and data is not as good far away from the peak pressure location. First, the model pressures for $1.28 < R_{OSP} < 1.32$ m are up to 50% below the measured value. This discrepancy could be due to the impact of the private region dome (which extends to $R \sim 1.28$ m) on recycling, which has been shown [22] to induce a long tail on the particle flux profile far from the separatrix. A higher baseline value in the second or far SOL region in table 1 (e.g. 0.05 MA m^{-2} instead of 0.025 MA m^{-2}) is needed to bring the model to a better agreement with the data. Second, the model falloff when $R_{OSP} > 1.4$ is faster than the data. The presence of a small baseline in the particle flux profile or a longer scale length in the PFR would lead to improved agreement here also. From a measurement standpoint, accurate determination of the profiles far from the separatrix can be difficult due to reduced signal/noise ratio. Thus the agreement between data and model is deemed sufficient for this study, noting that improved agreement probably requires profile measurements which must be optimized in the lower flux regions far into the SOL and in the PFR.

3.2. Inner divertor

The upper, inner divertor has an array of five domed Langmuir probes embedded in the centre post graphite tiles to provide measurements of the n_e, T_e and $\Gamma_{\parallel}$ profiles. Technically, the baseline model from [9] considered a strike point sweep in major radius. We note that the inner divertor case with the strike point sweep in height is analogous, except that the actual radius of the ion flux stays fixed along the vertical profile (used in the integrals in [9]), and that the incidence angle of the magnetic field on the centre post is defined by $\Theta_B(z) = \tan^{-1}[B_r(z)/B_\phi(z)]$.

The divertor profiles mapped into the $Z_{ISP} - Z_{probe}$ plane are plotted in figure 6, along with the fits used in the model
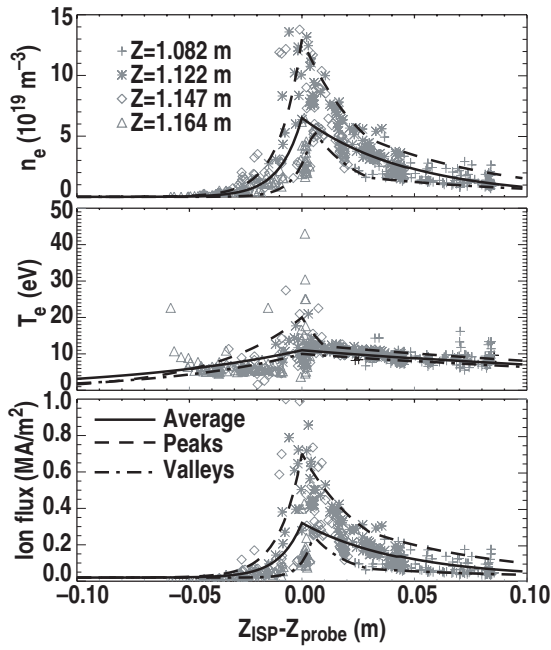
Figure 6. Inner divertor plasma profiles and fits mapped to the separatrix. The different symbols in the panels represent Langmuir probes at different vertical locations near the inner plenum. The three different curves through the data represent average (——), upper envelope (- - - -) and lower envelope (— · —) fits.

calculations below. Here Z_{ISP} is the ISP height off the midplane and Z_{probe} is the probe height relative to the midplane. The profile was fitted (least-squares) with exponential functions, similar to the fitting for the outer divertor profiles above, except that Z replaced R in equation (1) and that the SOL scale lengths are applied for $x < 0$ and the PFR scale lengths for $x > 0$. These fitted profile parameters are listed in table 3.

Note that the profiles in figure 6 display a large range. The upper part of the envelope corresponds to the profiles closest in time to the ELMs, whereas the lower part corresponds to the profiles furthest in time from the ELMs. Because the timescale of equilibration of this plenum (~4 ms) is just a few times larger than the average ELM duration, it is evident that the ELMs modulate the pressure gauge signal. To estimate this effect, the upper and lower envelopes of the data were reconstructed using the profile parameters in tables 4 and 5, with table 4 representing the near-ELM profiles and table 5 the between ELM profiles. Note that the upper and lower envelopes were not least-squares fitted profiles as in table 3 but were fit by visual inspection, which was deemed sufficient for this purpose. Note also that the upper and lower envelopes required two decay lengths on the SOL side to match the limits of the n_e and $\Gamma_\parallel$ profiles, but the fitted profile used only one because of the data scatter.

The other inputs needed for the model are the plenum entrance location (in this case, $Z_{cr} = 1.161$ m), plenum height $H = 0.04$ m and maximum strike point location (for the inner plenum, $Z_{max} \sim Z_{cr}$) in all cases, since the flux surfaces are horizontal when the ISP height approaches the size of the plenum opening. A comparison of the data and simulations using the average fits, and upper and lower envelopes of the plasma profiles is shown in figure 7. We note that the

ISP location (when on the side of the plenum opening) was extrapolated using $Z_{ISP} \sim Z_{pl} + 0.1(R_{ISP} - R_{centre\text{-}post})$, which means that the flux surface had a ~6° angle with respect to the vertical target. The computed pressure using the average fits from figure 6 (solid curve) lies mostly near the middle of the data range, except at maximum plenum pressure, where it lies near the top of the range. In addition, the average curve falls off a little more quickly than the data, as the ISP moves past the plenum opening. The pressure computed using the upper and lower envelopes of the plasma profiles (dash, dash-dot) effectively describes the pressure data. Overall, it can be seen that the agreement is quite reasonable, i.e. the model predicts the sharp increase in pressure as the ISP approaches the plenum, and the rather gradual falloff as the ISP becomes limited by the plenum opening. Physically, the rapid pressure increase from $Z = 1.1$–1.15 m corresponds to the sharp PFR scale length of the profiles sampled by the plenum as the ISP approaches the opening, whereas the gradual pressure falloff from $Z = 1.15$–1.18 occurs due to the sampling of the longer scale lengths by the plenum on the SOL side of the separatrix. However, we note that the computed upper band pressure is up to 100% above the data at peak pressure, and the computed lower band pressure can be 40% below data when the strike point is far away from the plenum. There are several possible reasons for the discrepancy. The most likely reason is that the equation used to compute pressure: $P_{pl} = I_{pl}/(S + C)$ is derived from a time-dependent flux balance, i.e. $dN_{pl}/dt = I_{in} - I_{out} - Q_{exh}$, where N_{pl} is the plenum neutral inventory, $I_{in} \equiv I_{pl}$ is the neutral flux into the plenum, I_{out} is the neutral leakage from the plenum into the main chamber and Q_{exh} is the cryopump exhaust rate. In a quasi-steady state, the following approximations are often used: $I_{out} = CP_{pl}$ and $Q_{exh} = SP_{pl}$, where C and S are the back conductance and pumping speed. Substituting for I_{out} and Q_{exh} and solving for the pressure yields $P_{pl} = I_{pl}/(S+C)$. It is relatively clear then that the upper envelope of the plasma profiles would lead to an overestimation of the pressure, since these profiles are governed by ELM effects which persist for a timescale shorter than the plenum timescale. By the same argument, however, it seems that the lowest set of profiles in figure 6 should be closer to the lower data range, since the persistence of the lower profiles is apparently long compared with the plenum timescale (figure 4). This latter discrepancy would vanish if the particle flux scale length were ~1.5 cm on the PFR side. While such a large PFR scale length is not apparent in the lowest data band in figure 6, it is noted that the probe signal/noise ratio is lowest at these low ion saturation currents, leading to a larger uncertainty in the precise width. A second possibility is that the upper and lower envelopes may change with time and the details of ELM size and recovery, whereas we used time-invariant profiles to compute the upper and lower bands.

4. Summary, discussion and conclusions

We have measured the characteristics of pressure rise in the upper inner and outer divertor plenums in DIII-D and now summarize observed similarities and differences. The upper outer plenum pumps the OSP flux, and the dependence of the pressure rise on distance from the strike point to the plenum

Table 3. Plasma profile parameters for inner plenum simulation—average (#101597).

Quantity	A_0	$\lambda_{SOL,1}$ (m)	$\lambda_{SOL,2}$ (m)	$\Delta_{SOL,1}$ (m)	λ_{PFR} (m)	Δ_{sep} (m)	B_0
$\Gamma_{\parallel}$ (MA m^{-2})	0.32	0.044	—	—	0.01	0	0.02
n_e (10^{19} m^{-3})	6.5	0.047	—	—	0.01	0	0
T_e (eV)	11	0.22	—	—	0.05	0	0

Table 4. Plasma profile parameters for inner plenum simulation—peaks (#101597).

Quantity	A_0	$\lambda_{SOL,1}$ (m)	$\lambda_{SOL,2}$ (m)	$\Delta_{SOL,1}$ (m)	λ_{PFR} (m)	Δ_{sep} (m)	B_0
$\Gamma_{\parallel}$ (MA m^{-2})	0.7	0.03	0.06	0.03	0.01	0	0.02
n_e (10^{19} m^{-3})	13	0.03	0.06	0.03	0.01	0	0
T_e (eV)	10	0.01	—	—	0.01	0	9.5

Table 5. Plasma profile parameters for inner plenum simulation—valleys (#101597).

Quantity	A_0	$\lambda_{SOL,1}$ (m)	$\lambda_{SOL,2}$ (m)	$\Delta_{SOL,1}$ (m)	λ_{PFR} (m)	Δ_{sep} (m)	B_0
$\Gamma_{\parallel}$ (MA m^{-2})	0.28	0.016	0.06	0.03	0.01	0.005	0.02
n_e (10^{19} m^{-3})	5.5	0.02	0.08	0.03	0.007	0.005	0
T_e (eV)	10	0.22	—	—	0.05	0	0
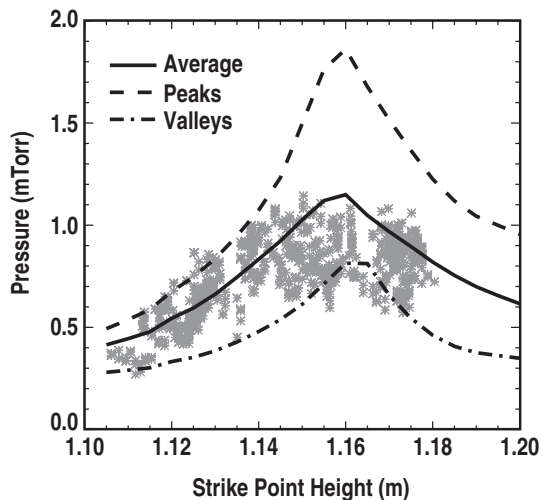
Figure 7. Simulation of the inner plenum pressure during the ISP sweep, using the average (——), upper envelope (- - - -) and lower envelope (— · —) fits from figure 6. The upper envelope represents pressure gauge signal near ELMs and the lower envelope far from ELMs.

opening is similar to the lower outer plenum. The upper inner plenum, on the other hand, pumps the ISP flux and has both a smaller volume and time constant than the outer plenum. As a result, the pressure measurement is modulated by nearly a factor of two, in phase with ELMs. Finally, the upper inner plenum pressure increases more quickly than that of the outer plenum as the strike point approaches the plenum opening and falls off more slowly as the strike point moves on to the side of the opening. This effect occurs because the inner plenum samples the PFR flux first, which has smaller decay lengths than the SOL flux, followed by the flux in the near separatrix region and then the flux in the SOL, i.e. in the opposite order compared with the upper outer plenum.

We have shown that simulations of the dependence of plenum pressure on strike point location are generally in good agreement with measured neutral pressures in the upper inner and outer plenums in DIII-D. The analytic model used Langmuir probe divertor profiles and EFIT equilibrium reconstructions as inputs. The outer plenum pressure data can be modelled using plasma profiles averaged over ELMs, due to the long time constant of the plenum relative to the fast timescale of ELMs. It is conspicuous that the particle flux profiles with the R_{OSP} near the private region dome develop a baseline in the far SOL, which leads to enhanced neutral flux and pressure in the plenum. The simulations have been shown to be sensitive to the presence of such baselines. The modelling of inner plenum pressure with the time-averaged profile largely traces through the bulk of the pressure data. Simulation with two additional sets of profiles: one upper envelope set ('near ELMs') and one lower envelope set ('far from the ELMs', see figure 6), reproduces the bands of the pressure measurements, although the model calculations using the peak (valley) profiles can be too high (low) for certain strike point locations. This discrepancy is attributed to the time dependence of the profiles themselves and the short baffle time constant. The generally good agreement between model and data corroborates the use of such models in plenum data interpretation. The major limitation of this model is the inability to predict changes to the SOL profiles due to the addition of material surfaces. Thus, the use of this model in conjunction with a predictive two-dimensional edge plasma and neutral transport code, e.g. UEDGE or B2.5, may provide an alternate, time-efficient method for future plenum design calculations.

Acknowledgments

out that $R_{max} \sim R_{cr}$ when the strike point is far away from the plenum opening, leading to a revision of the original model. Finally, we thank the referees for their careful reading of the manuscript and encouragement for further studies.

References

[1] Mahdavi M.A. *et al* 1993 *Proc. 20th Euro. Conf. on Controlled Fusion and Plasma Physics* vol 17C (Petit-Lancy, Switzerland: European Physical Society) p II-47
[2] Allen S.L. 1999 *J. Nucl. Mater.* **266–269** 168
[3] Mahdavi M.A. *et al* 2001 *J. Nucl. Mater.* **290–93** 905
[4] Mioduszewski P.K. *et al* 1995 *J. Nucl. Mater.* **220–222** 91
[5] Maingi R. *et al* 1997 *J. Nucl. Mater.* **241–243** 672
[6] Colchin R.J. *et al* 1999 *J. Nucl. Mater.* **266–269** 472
[7] Klepper C.C. *et al* 1993 *Nucl. Fusion* **33** 533
[8] Maingi R. *et al* 1995 *J. Nucl. Mater.* **220–222** 320
[9] Maingi R. *et al* 1999 *Nucl. Fusion* **39** 1187
[10] Corbett W.J. *et al* 1991 *Nucl. Fusion* **31** 1067
[11] Loarte A. *et al* 1997 *Proc. 24th Euro. Conf. on Controlled Fusion and Plasma Physics (Berchtesgaden)* vol 21A (Geneva: European Physical Society) p III-1049
[12] Allen S.L. *et al* 1999 *Nucl. Fusion* **39** 2015
[13] Mahdavi M.A. *et al* 1981 *Phys. Rev. Lett.* **47** 1602
[14] Haas G. *et al* 1984 *J. Nucl. Mater.* **121** 151
[15] Klepper C.C. *et al* 1993 *J. Vac. Sci. Technol.* A **11** 446
[16] Haas G. and Bosch H.-S. 1998 *Vacuum* **51** 39
[17] Menon M.M. *et al* 1992 *Fusion Technol.* **22** 356
[18] Haas G. *et al* 1999 *J. Nucl. Mater.* **266–269** 1065
[19] Lao L.L. *et al* 1985 *Nucl. Fusion* **25** 1611
[20] Watkins J.G. *et al* 2003 *J. Nucl. Mater.* **313–316** 1258
[21] Buchenauer D.N. *et al* 1990 *Rev. Sci. Instrum.* **61** 2873
[22] Watkins J.G. *et al* 2001 *Bull. Am. Phys. Soc.* **46** 225